Delft University of Technology

Experimental study and discrete element analysis on dynamic mechanical behaviour of railway ballast bed in windblown sand areas

Xiao, Hong; Zhang, Zhihai; Chi, Yihao; Wang, Meng; Wang, Haoyu

Important note
To cite this publication, please use the final published version (if applicable).
Please check the document version above.

Experimental study and discrete element analysis on dynamic mechanical behaviour of railway ballast bed in windblown sand areas

Hong Xiao [a,b,*], Zhihai Zhang [a,b], Yihao Chi [a,b], Meng Wang [c], Haoyu Wang [d]

[a] School of Civil Engineering, Beijing Jiaotong University, Beijing 100044, China
[b] Beijing Key Laboratory of Track Engineering, Beijing Jiaotong University, Beijing 100044, China
[c] China Academy of the Railway Sciences Co., Ltd., Beijing 100081, China
[d] Engineering Structures Department, Delft University of Technology, the Netherlands

ARTICLE INFO

ABSTRACT

Due to the limitation of the geological environment, many railways around the world are built in desert areas. The intrusion of sand particles can increase the stiffness of ballast beds and cause corrosion and fracture of fasteners, turnout blockage, etc., even affecting the service safety of railways. In the paper, based on the results of field and laboratory tests, a three-dimensional discrete element model of the sandy ballast bed is developed to study the effect of sand intrusion on the load sharing ratio of sleepers, contact forces between ballast particles, displacements of ballast particles, and energy dissipation in ballast beds. The results show that the axle load in sandy tracks is mainly shared by three sleepers under the single-axle load and six sleepers under the dual-axle load. The maximum contact force under the sleeper in the sandy ballast bed is about 80% larger than that in the clean ballast bed and its normal and tangential contact forces are also larger than that in the clean ballast bed. The ballast particles at the ballast shoulder of the clean ballast bed move downward in the direction of less than 45°, while those in the sandy ballast bed move outward at the direction of 90°. The sand intrusion inhibits the movement of ballast particles and may cause a rheological phenomenon of ballast particles at the ballast shoulder. The intrusion of sand particles mainly affects the elastic strain energy and damping energy in ballast beds but has less effect on friction energy and kinetic energy.

1. Introduction

The ballast bed in railways is formed by stacking and compacting crushed stones with various sizes of particles. Its functions include bearing and transferring sleeper pressure, keeping the lateral and longitudinal stability of track, as well as absorbing wheel-rail vibration [1,2]. To transport goods and people, the railways in most countries in the Middle East and Asia have to be built in desert areas. In those areas, frequent sandstorms challenge the service quality of railway structures (especially the ballast layer) [3,4,38]. Fig. 1 shows the distribution of major railway lines crossing desert areas in China.

Because there are a large number of voids between ballast particles in ballast beds, the material with small particle sizes can intrude in the voids and gradually deposit due to trainloads and environmental issues. Selig et al. [1] has found that the ballast bed fouling caused by the crushing and pulverization of ballast particles and the intrusion of external fine particles from the upper surface of the ballast bed is the main source of the total pollution, which accounts for 83%, as shown in Fig. 2 (a). In addition, studies [1,2,4] have shown that the fouling material could significantly change the mechanical properties of ballast beds, wherein the effect on the shear strength of the ballast bed is most significant. When the fouling developed to a certain extent, it could seriously affect the mechanical behaviour of the ballast bed, even resulting in mud pumping and ballast hardening. The windblown sand is typical fouling in ballast beds. The continuous intrusion of sand particles changes the gradation of ballast, and therefore changes the contact between ballast particles and the force chain distribution, as shown in Fig. 2 (b) and (c). Eventually, many diseases can happen to the track, such as arch in the longitudinal level, corrosion of fastener, depressed joint, twist warp, etc., which not only deteriorate the track geometry, service life and mechanical properties of ballast beds, but also increase the workload of track maintenance [3,5,39]. Therefore, it is important to study the mechanical behaviour of the ballast beds with windblown sands.

To understand the mechanical behaviour of the ballast beds with windblown sands, many experimental and numerical studies have been conducted.

(1) Experimental research

Tolou Kian et al. [4,6] analyzed the effect of sand content on the static mechanical behaviour of ballast beds such as shear strength and deformation modulus, by conducting large-scale direct shear tests and plate load tests in the laboratory. The results showed that sand intrusion reduced the shear strength and shear angle of the ballast bed, and when sand content exceeded a limit, the deformation modulus of the ballast bed decreases sharply. Zakeri et al. [7–8] analyzed the influence of sand intrusion on the bending moment and load sharing ratio of a single sleeper through a field test of measuring sleeper bottom pressure in a windblown sand railway. They suggested using the hump slab tracks instead of conventional ballast beds to avoid the phenomenon of sand filling the voids in ballast beds. Koohmishi [9] and Tennakoon et al. [10] studied the influence of grading of ballast and fouling materials (including coarse sand and fine sands) on the drainage capacity of ballast beds. In addition, a series of large-scale drainage capacity tests were conducted to study the relationship between the porosity and drainage capacity of ballast beds under various sand contents. Ionescu et al. [11] studied the deformation and degradation of ballast beds with windblown sands by laboratory tests. The research results of Selig and Waters [1] showed that sands and fine-size gravels can increase the shear strength and stiffness of ballast beds as long as the coarse ballast particles still form the ballast skeleton. Esmaeili et al. [12,13] tested the track stiffness and sand content in a desert railway line. The results showed that the track stiffness gradually grew with the increase of sand content. When the sand content was 62.7%, the track stiffness increased to 116 MPa, which was 5.9 times larger compared to that of the clean track. Furthermore, they added 0%, 5%, 10% and 15% TDA (Tire Derived Aggregates) into the ballast samples with various sand content (0%, 50% and 100%, respectively) and carried out 36 cyclic uniaxial loading tests to study the settlement, crushing and damping ratio in the ballast samples. The results showed that with the increase of sand content, the damping ratio of ballast samples decreased gradually, while the cumulative settlement and crushing proportion of ballast increase gradually. The research results of Tyfour et al. [14] indicated that sands could fill the voids between ballast particles to hinder the movement of particles, thus increasing the track stiffness and damping. Besides,

moisture has a significant effect on the mechanical behaviour of the ballast bed with windblown sands. Studies in [21] have shown that when the water content is between 0 and 15%, the ballast with windblown sands stabilized in a shorter loading period, while as the water content increasing, the stiffness of the ballast bed experiences a process of increase–decrease-increase–decrease (slowly) and 10% water content was the critical point of stiffness change. Sadeghi et al. [38,39] showed that wet sands could reduce the shear strength and stiffness of the ballast bed by conducting the laboratory test, while the geogrid could enhance the shear strength and vertical stiffness of the ballast bed with windblown sands. Zhang et al. [40] conducted the field test on the vertical stiffness of the ballast beds with windblown sand (saturated sand particles in ballast voids). The results showed that the average vertical stiffness of the ballast beds was 48.95% higher than that of clean ballast beds.

The above experimental research mainly focuses on the static behaviour of the ballast beds with windblown sand, such as shear strength, deformation and drainage capacity, while the dynamic behaviour under train load has been less studied. Moreover, most of the existing laboratory tests overlooked the effect of sand intrusion on sharing ratio of sleepers, wherein a constant load has been used in the tests. However, there is a load of change in the actual working condition of the railway lines in sandy areas.

(2) Numerical simulation

Esmaeili et al. [12] analyzed the influence of sand content on the acceleration and displacement of track structure using the finite element method (FEM). The results showed that the maximum acceleration of the track structure increased by about 43%, while maximum displacement decreased by about 68% as the sand content increasing from 0% to 62.7%. Zakeri et al. [15] developed a two-dimensional finite element model of the track with windblown sands using the ABAQUS software to study the variation of vertical displacement, velocity and acceleration of track structure. In the simulation, the various sand content is modelled by changing the stiffness of the ballast bed. Tolou Kian et al. [16] developed a three-dimensional finite element model of ballast track to study the influence of ballast with windblown sands on the design of sleepers and proposed a new design of concrete sleepers. Huang et al. [43] developed a fouling ballast bed model with half sleeper length using the discrete element method (DEM). The coal powder content was modelled by adjusting the contact parameters between ballast particles.
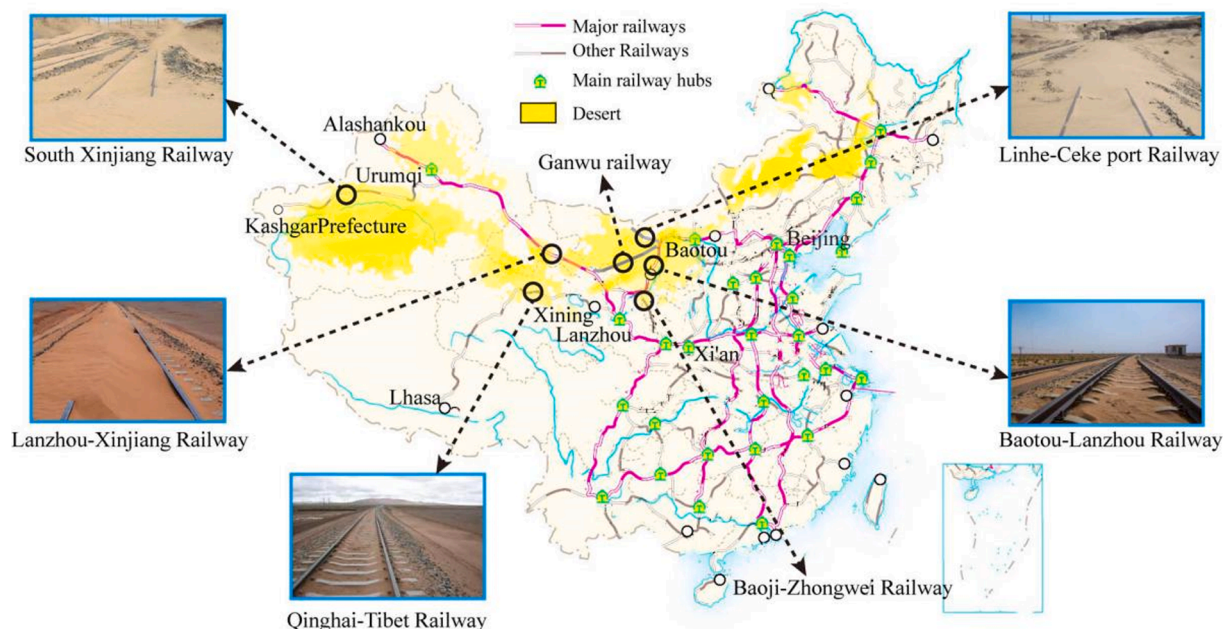

Fig. 1. Distribution of windblown sand railway lines in China.

The influence of the content and position of the fouling material on the settlement of the ballast bed was studied. Ngo et al. [45] used the discrete element method to study the influence of geogrid on the mechanical behaviour of the ballast beds with coal powder. The results showed that coal powder intrusion could reduce the interlocking between ballast particles and geogrid, thereby reducing the shear strength. From the above research, the finite element method has been used mostly to study the railway tracks with windblown sands. However, because the finite element method is based on the continuum assumption, the interaction between sand particles and ballast particles cannot be considered accurately. Besides, although some studies of coal power used the discrete element method, the mechanical behaviour of the ballast beds with sand intrusion still needs to be researched, due to the great differences between the two fouling materials.

To study the mechanical behaviour of the ballast beds with windblown sands, the field test of load sharing ratio of sleepers is firstly conducted in a severe sandy section (saturated sand particles in ballast voids) and a clean section in China. After that, the contact parameters between sand particles are calibrated by repose angle tests in the laboratory. Finally, considering the multi-scale effect between sand particles and ballasts, a three-dimensional discrete element model of the ballast bed with windblown sands is developed for the first time. Using the model, the effect of sand intrusion (saturated state) on the dynamic mechanical behaviour and energy dissipation of the ballast bed is analyzed at both the macroscopic and mesoscopic perspectives. The results provide theoretical guidance for the optimization of the structure and maintenance scheme of railways in desert areas.

2. Material and method

2.1. Test object

The field test has been conducted in a clean section and a highly sandy section of track in China, as shown in Fig. 3 (a) and (b). The design of the Class I railway in China is shown in Fig. 4 (a) [17]. The ballast material is crushed stones made of basalt. The Los Angeles abrasion (LAA) rate of the ballast particles is 23%, the standard aggregate impact toughness IP is 97, and the compressive strength of the stone powder specimen is 0.3 MPa [18]. The track structure is composed of the CHN60N rail (60.64 kg/m), the clip type II fastener and the new type II concrete sleeper (the length is 2500 mm). The sleeper spacing is 0.6 m. The ballast grading is shown in Fig. 4 (a). The top width of the ballast bed is 3.5 m, the thickness is 0.35 m, and the slope is 1:1.75 [19], as shown in Fig. 4 (b) and (c).

During the test, the speed of trains is about 45 km/h. The types of locomotives are the DF_49529 and DF_49601 with a wheel distance of 1800 mm and an axle load of 23 t, as shown in Fig. 3 (c) and (e). The type of freight wagons is the C70E with a wheel distance of 1830 mm, a bogie distance of 9210 mm and an axle load of 23 t, as shown in Fig. 3 (d) and (e).
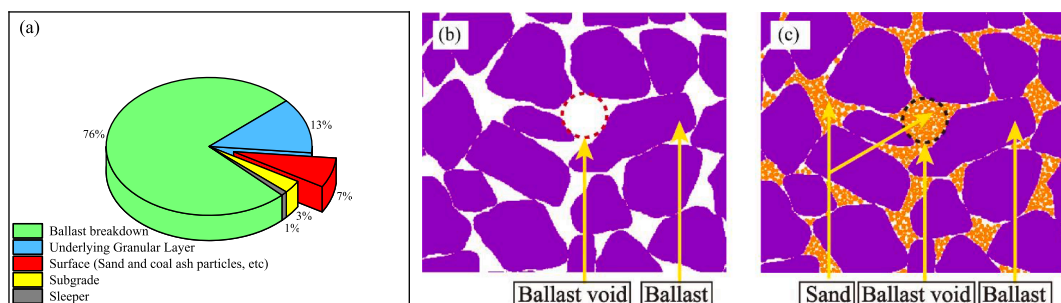
2.2. Test method

2.2.1. Test of load sharing ratio of sleepers

Based on the Winkler foundation model, Lv et al. [20] assumed that the track is a linear elastic continuum that uniformly distributed and proposed the relationship between the load sharing ratio of sleepers and Gauss distribution, and got the approximate calculation method of the sharing ratio α_i. The calculation Equation is as follows:

$$\alpha_i = e^{-\frac{x_i^2}{2\sigma^2}} / \sum_{i=1}^{n} e^{-\frac{x_i^2}{2\sigma^2}} \qquad (1)$$

where σ is the shape function, i is the number of sleeper bearing wheel loads, and x_i is the coordinate of the Sleeper i reference to the contact point of the wheel load. When the wheel force applies on directly above, n = 5, while that between sleepers, n = 6. Based on the assumption that the track is a linear elastic continuum, the displacement of sleepers is used to analyze the influence range of sand intrusion on the wheel load and the load sharing ratio of sleepers.

Considering the actual situation of clean and sandy sections of railway track and existing research results in [7,20], three high-precision displacement sensors have been installed on each sleeper, and 7 sleepers are measured (21 displacement sensors in total). All the displacement sensors have been connected to the data acquisition instrument by cables. The field setup is shown in Fig. 5. The number of displacement sensors is shown in Fig. 6 (a), where the sensors at the sleeper end in the clean section are referred to as "CDL" and "CDR" respectively and the sensors at the sleeper center "CDC". In the same way, the sensors at the sleeper end in the sandy section are referred to as "SDL" and "SDR" respectively, and the sensors at the sleeper center "SDC".

2.2.2. Test of sleeper pressure and ballast acceleration

Considering that the discrete element method will be employed to study the influence of sand intrusion on the dynamic mechanical behaviour of the ballast bed under train loads, the sleeper pressure of Sleeper 4 (the pressure transmitted by rail to sleeper) and the acceleration of the ballast bed are measured, as shown in Fig. 6 (a) and 6 (b). The resolution of the acceleration sensor is 501 mv/g (test conditions: 21°C, 160 Hz, 1 g), with the measuring range of 10 g, the shock resistance of 500 g, the resonant frequency of 16 kHz, the frequency range of 0.35–5000 Hz, and the bias voltage of 8-12VDC. The test results of sleeper pressure are mainly used as the input of load applied in the discrete element model, while the test results of acceleration in the ballast bed to validate the discrete element model.

3. Results and analysis of the field test

3.1. Single-axle load

Since the railways in the desert area are affected by the harsh environment during operation, trains often run with a speed limit. In order to

Fig. 2. Ballast fouling: (a) Fouling material; (b) Voids in ballast bed; (c) Voids filled by sands.
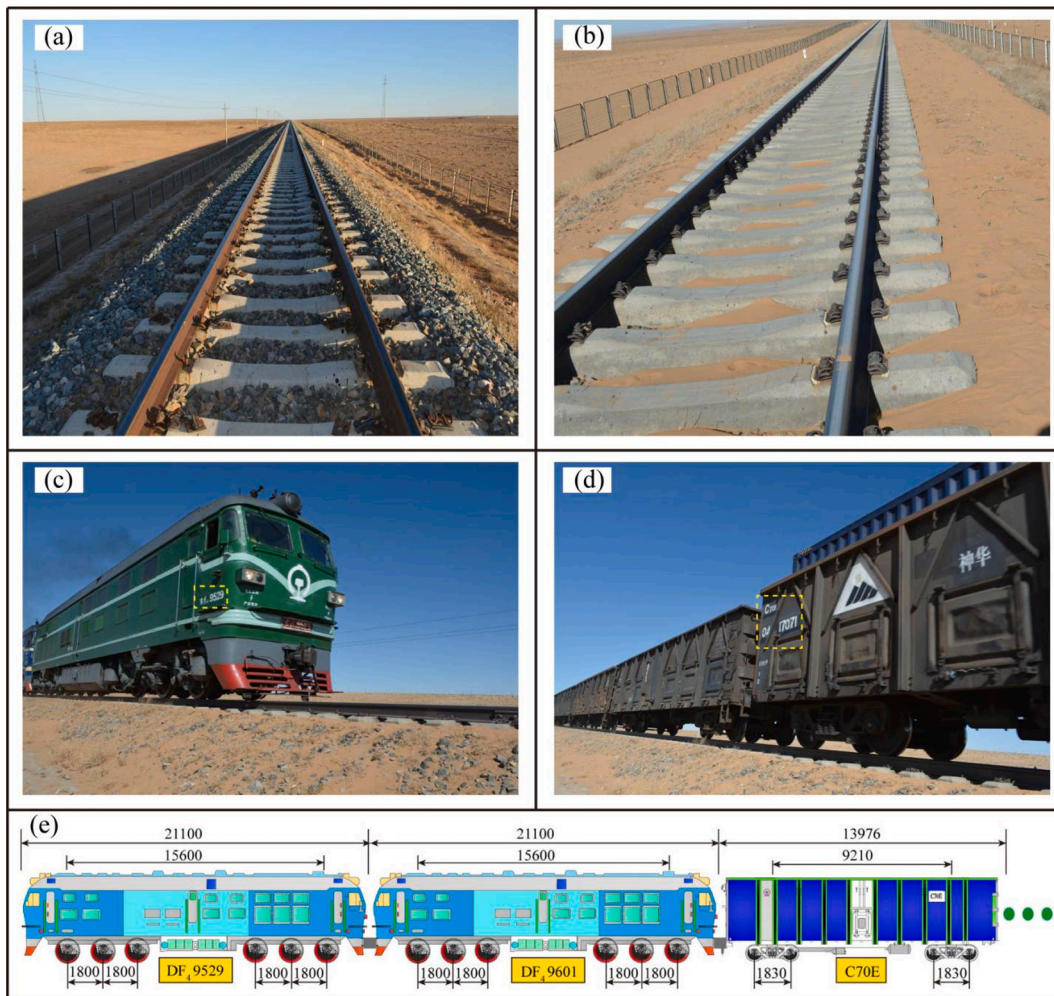
Fig. 3. Field test: (a) Clean railway, (b) Sandy railway, (c) Locomotive, (d) Freight wagon, (e) Train formation (Unit: mm).
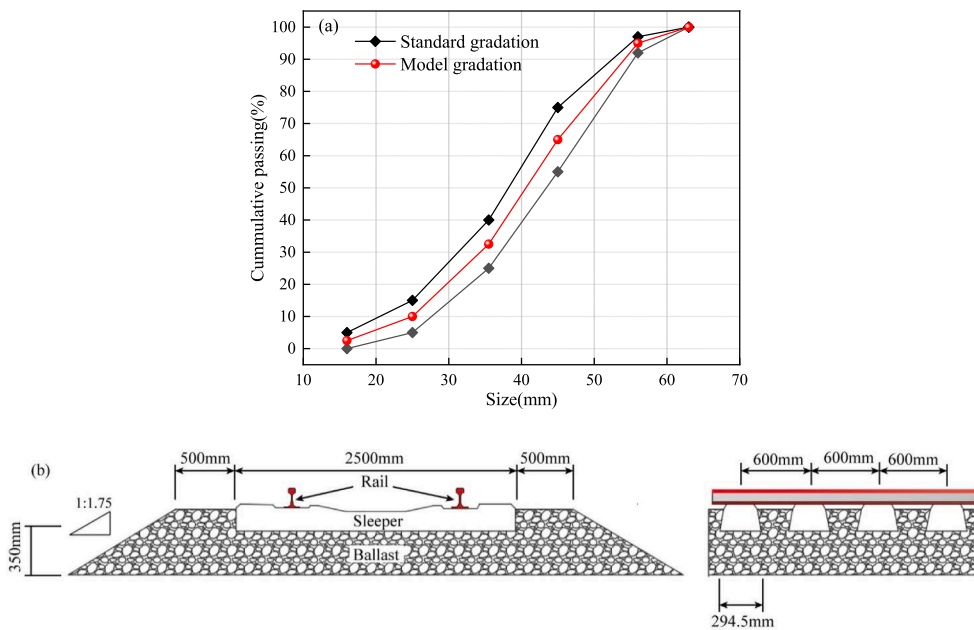

Fig. 4. Tested track structure: (a) Ballast grading, (b) Track structure.
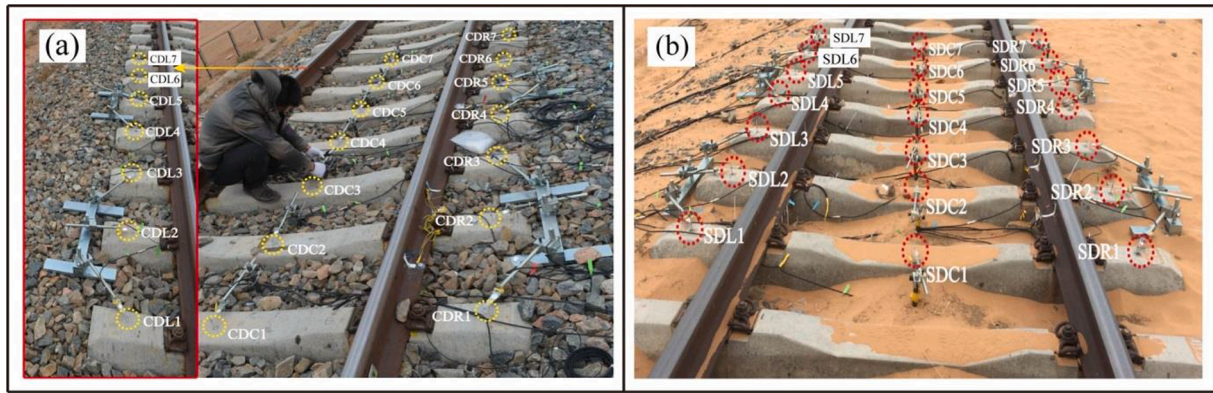
Fig. 5. Installation of test equipment: (a) Clean ballast bed, (b) Sandy ballast bed.
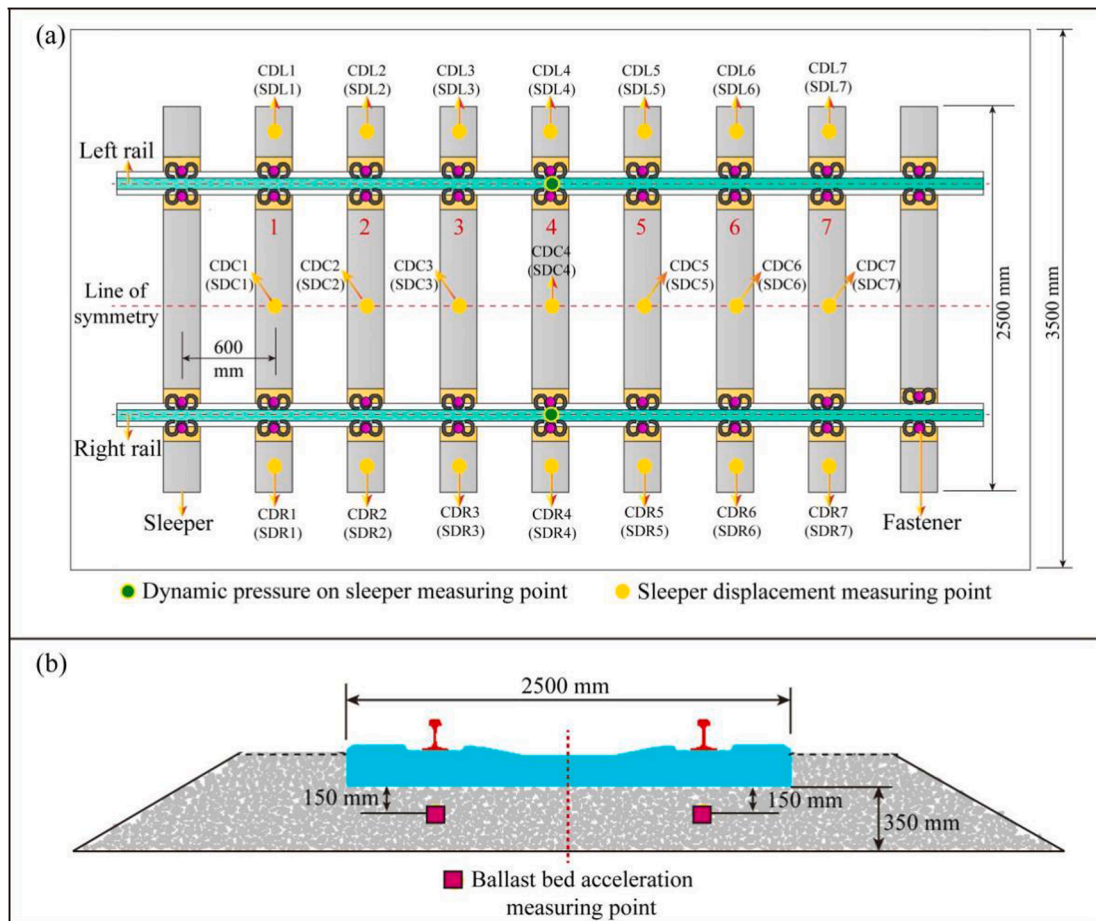

Fig. 6. Layout of measuring points: (a) Plan view, (b) Side view.

study the influence of sand intrusion on the load range of a single-axle load, the transfer process of the single-axle load at the speed of 45 km/h is analysed as an example. Because the wheel loads acting on the rail is always in a group, the load sharing ratio of sleepers can be affected by the adjacent axle or bogie. To solve the problem, the time when the last axle of the last train passes right above the Sleeper 1 is taken as a benchmark in the data processing procedure. The average displacements of 7 sleepers under 10 train loads are obtained as shown in Fig. 7.

As seen from Fig. 7, the displacement of the Sleepers 1, 2 and 3 in the clean section and sandy section are large, while the displacements of the Sleepers 4, 5, 6 and 7 are nearly zero. Therefore, it can be preliminarily concluded that the influence range of a single-axle load is close to the

length of 5 sleepers, which is consistent with the findings in [20]. The calculation of load sharing ratio of sleepers under a single-axle load is expressed as follows:

$$\beta_i = \frac{D_i}{\sum_{i=1}^{n} w_i D_i} \tag{2}$$

where β_i is the test result of load sharing ratio of sleepers, i is the sleeper number, D_i is the dynamic displacement of sleeper numbered i under the peak of the load, n is the number of sleepers within the influence range, and w_i is the weight of sleeper displacement, which is usually taken as 1. According to the linear elastic assumption of the track, the displacements of Sleepers 2 and 3 are mirrored with respect to the center line of
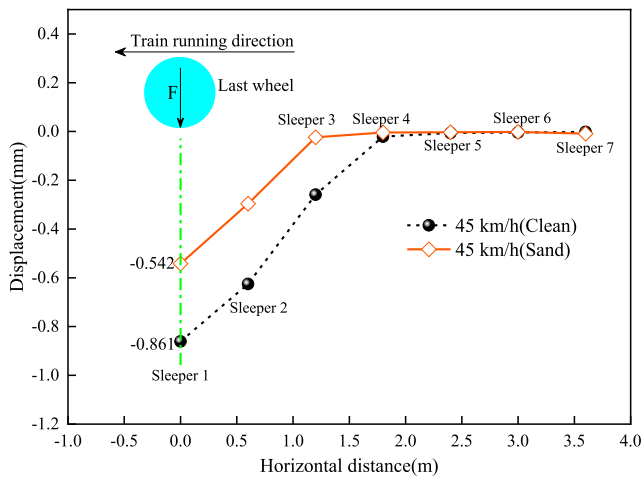
Fig. 7. Sleeper displacement under single-axle load.

Table 1
Load sharing ratios of sleepers under single-axle load.

Section type	Load sharing ratios of sleepers				
	Sleeper 3′	Sleeper 2′	Sleeper 1	Sleeper 2	Sleeper 3
Clean	8.92%	24.31%	33.54%	24.31%	8.92%
Sandy	2.06%	25.01%	45.86%	25.01%	2.06%
Difference	−6.86%	0.70%	12.32%	0.70%	−6.86%

Sleeper 1, therefore, the displacement of Sleepers 2′ and 3′ can be obtained. The load sharing ratio of sleepers under a single-axle load calculated by Eq. (2) is shown in Fig. 8 and Table 1.

As seen from Fig. 8 and Table 1, the single-axle load is mainly borne by 5 sleepers in the clean section, with their load sharing ratios of 8.92%, 24.31%, 33.54%, 24.31% and 8.92%, respectively. However, the load sharing ratios of sleepers in the sandy section are different, which are 2.06%, 25.01%, 45.86%, 25.01% and 2.06%, respectively. The load sharing ratio of the center sleeper (Sleeper 1) is 1.95 times larger than that of Sleepers 2′ and 2, 22.26 times than that of Sleepers 3′ and 3. The sum of the load sharing ratio of the sleepers at two ends (Sleeper 5′ and 5) is less than 5%, which is 4.12%. This shows that the single-axle load is mainly carried by three sleepers in the sandy section, and the center sleeper bears a greater load. The reason is that when the sand fills the voids in the ballast bed, the stiffness of the ballast bed is increased and thus the track deformation under axle load is reduced. As a result, the range affected by the axle load becomes short in the longitudinal direction of the track. In addition, compared with the clean section, it is found that the center sleeper in the sandy section carries a larger load, since the load sharing ratio of Sleeper 1 increasing by 12.32%, while that of the adjacent sleepers increasing only by 0.7% and that of the furthest sleepers decreasing by 6.86%. It shows that the sand intrusion leads to a reduction in track elasticity, which is unfavourable to the distribution of wheel force. In summary, the sand intrusion can change the load sharing ratios of sleepers, so that the force applied on sleepers is significantly

increased under the wheel and the part of the forces carried by the sleepers away from the wheel shift to the sleeper under the wheel, which is similar to the results in [7]. The reason is that the intrusion of sand particles fills the voids in the ballast bed, hindering the movement of ballast particles, and thus reducing the displacement of the sleeper under the load and changing the transfer mechanism of wheel loads.

To further analyze the influence of sand intrusion on the load range, the approximate calculation equation of the load sharing ratio of sleepers under a single-axle load is fitted by a nonlinear function, as shown in Eq. (3).

$$y_i = a \times \frac{1}{b\sqrt{2\pi}} e^{-\frac{(x_i - x_0)^2}{2b^2}} + c \qquad (3)$$

where y_i is the approximation of the load sharing ratio of the ith sleeper, a is the variation coefficient of amplitude, b is the standard deviation; x_0 is the position of the single wheel, and c is the adjustment coefficient of the load sharing ratio. According to Fig. 8 and Eq. (3), the sand intrusion leads to the increase of the coefficient a, while a reduction in b and c, resulting in the ratio of a/b growing and consequently changing the load sharing ratio of sleepers. The coefficient b in Eq. (3) indicates the phenomenon that sleeper force in the loading range concentrates to the sleeper under the load, and the greater the value of b, the stronger concentration is. The coefficient a and the ratio a/b can reflect the load carried by the center sleeper, and the larger the value, the larger load carried by the sleeper is. The coefficient c is closely related to the change of load sharing ratio of sleepers at the ends and can be used to adjust the load sharing ratio of sleepers at the ends.

To summarise, the sand intrusion changes the load distribution in the track and the axle load in the sandy section is mainly carried by three sleepers. According to Table 1, the load sharing ratios of sleepers 3′ and 3 in the sandy section (not more than 5%) can be ignored and the updated sharing ratios to three sleepers are 26%, 48% and 26%, respectively, which is 1.3:2.4:1.3. Therefore, it is suggested that the increase of loads on sleepers should be properly considered in the track design of the railways in desert areas.
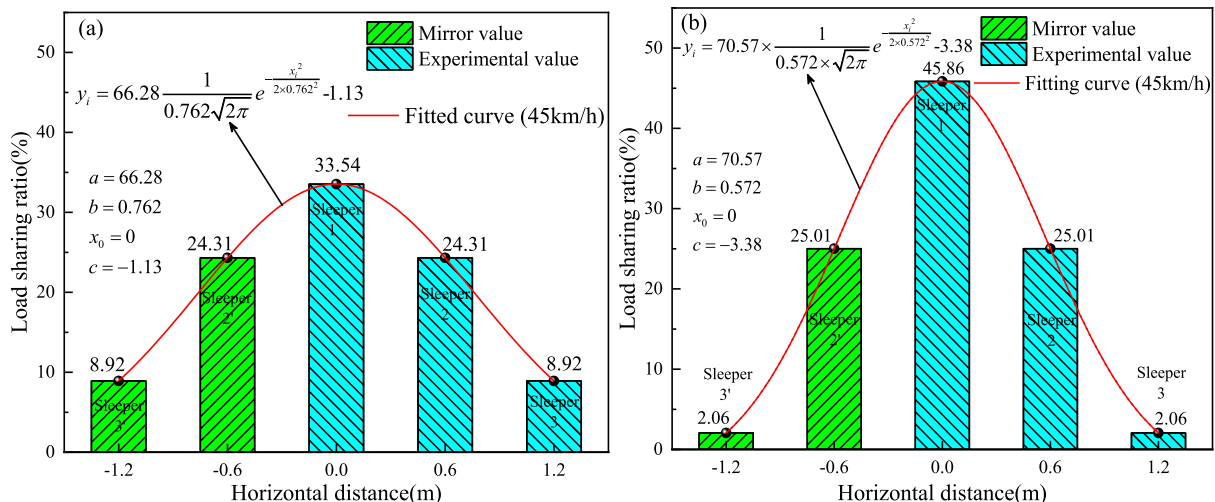

Fig. 8. Load sharing ratios of sleeper under a single-axle load: (a) Clean section (45 km/h); (b) Sandy section (45 km/h).

3.2. Dual-axle load

The dual-axle load (a bogie) is the most basic form of load combination, and thus must be considered in the design of subgrade structure to calculate subgrade stress. To study the influence of sand intrusion on the load sharing ratio of sleepers under the dual-axle load, the last bogie of the last train is considered. Referring to the analysis of the single-axle load, the displacements of sleepers are obtained in two steps. In the first step, the displacements of sleepers are recorded when the front wheel of bogie (Wheel A) is at 30 mm to the left of the centerline of Sleeper 1 and the rear wheel (Wheel B) is just above Sleeper 4. In the second step, the displacements of sleepers are also recorded when Wheel A is directly above Sleeper 1 and the rear Wheel B is at 30 mm to the right of the centerline of Sleeper 4. Since Wheel A and B are symmetric with the centerline of the bogie, the displacements of Sleeper 5, 6 and 7 in the second step are symmetrical to the grey area on the left side of Sleeper 1 (Area R) and marked as Sleeper 5 ', 6 ' and 7 ', respectively. After that, the displacements of sleepers recorded in two stages are combined to obtain the displacement curve of sleepers under the dual-axle load, as shown in Fig. 9.

As seen from Fig. 9, the displacements of Sleepers 7 and 7′ are nearly 0 mm, while the displacements of other sleepers are larger. Thus, it can be seen that the loading ranges of the dual-axle load on the clean and sandy sections are both less on 8-sleeper long. The load sharing ratio of sleepers is calculated according to Eq. (2) and shown in Fig. 10.

Fig. 10 shows that the load sharing ratio of sleepers shows an "M" shape under the dual-axle load in both the clean and sandy sections. The load sharing ratio is relatively larger near the axles while smaller far from the axles. In addition, the comparison shows that the sand intrusion increases the load sharing ratio close to the axles and decreases the load sharing ratio far away from the axles. For further analysis, the load sharing ratios of sleepers in both sections are compared in Table 2.

As seen from Table 2, the load sharing ratios of sleepers in the clean section under the dual-axle load are 8.51%, 25.78%, 35.62%, 29.89%, 31.83%, 36.51%, 25.56% and 6.21%, respectively, which are all larger than 5%. Therefore, the loads in the clean section are mainly carried by 8 sleepers. Differently, the load sharing ratios of sleepers in the sandy section are 2.98%, 25.69%, 46.21%, 24.02%, 26.22%, 47.52%, 24.99% and 2.37%, respectively. Because the sharing ratios of Sleepers 6′ and 6 that are far away from the axles are both less than 3%, they can be ignored. Hence, the loads in the sandy section are carried by 6 sleepers. Through further comparison, it is found that the load sharing ratios of the sleepers near the wheels (Sleeper 1 and 4) increase by 10.50% and 11.01%, respectively, while that of the sleepers between axles (Sleepers 2 and 3) decrease by 5.87% and 5.61%, respectively. The sharing ratios of the sleepers at the outer side of axles (Sleeper 5′ and 5) decrease by 0.09% and 0.57% and that of the sleepers far away from the axles (Sleepers 6′ and 6) decrease by 5.53% and 3.84%. It shows that sand particles have a strong influence on the load sharing ratio of sleepers in the sandy sections under the dual-axle load, which is the increase of the

load sharing ratio of the sleepers near the axles. This is because the sand intrusion increases the support stiffness of the ballast bed under the sleeper, changing the transmission path of contact force between ballast particles, resulting in the increase in the contact area between sleepers and the ballast bed and changes in the mechanical state of sleepers.

Ignoring the load sharing ratios of Sleepers 6′ and 6 and redistributing the load sharing ratio to the 6 sleepers, the load sharing ratio of sleepers in the sandy section under the dual-axle load can be updated, which are 26%, 47%, 25%, 27%, 49%, and 26%, respectively, approximating to 2.6:4.7: 2.5:4.9:2.6. Compared with ratios under the single-axle load (Table 1), the load sharing ratio of the sleeper under the axle raises by about 1.66%. Therefore, it is suggested to consider the dual-axle load in the design of the track structure to calculate of influencing the depth of dynamic load in subgrade in sandy railway track. Besides, the effect of sand intrusion on the load sharing ratio of sleepers should also be considered.

4. Numerical simulation

4.1. Ballast bed model using the discrete element model

The ballast particles in ballast beds have remarkable anisotropy in various shapes and sizes. The previous studies in [22–23] show that the shape of ballast particles has a great influence on the mechanical properties of ballast beds. Therefore, the precise modelling of the shape of ballast particles is the key to ensure high accuracy of the calculation. Thus, the laser scanning method is used to obtain the three-dimensional contour of irregular ballast particles. The modelling of ballast particles follows the studies in [23,32,43], wherein all ballast particles are considered as unbreakable bodies and generated by the filling method of multiple clump elements. The specific generation process of a ballast particle is shown in Fig. 11. Considering the calculation efficiency, the 34-ball element is used in the study as indicated by the red dashed box in Fig. 11.

Due to the large number of sand particles and the great difference between the size of sand and ballast particles, the calculation can be extremely time-consuming. To deal with the convergence problem during the calculation, only the most important part in the track (A1 and A2) is modelled comprehensively considering the difference between the confining pressure of the side slope of the track bed and the longitudinal and lateral confining pressure of the line, as shown in Fig. 12. It is because the part covers the areas of high sleeper pressure as well as the slope of the ballast bed. The software used is PFC 3D. The ballast grading in the clean ballast bed (Fig. 12 (b)) and the sandy ballast bed (Fig. 12 (c)) both adopt the red curve in Fig. 4 (a). The thickness of the ballast bed is 350 mm and the new type II concrete sleeper is used. The train load is applied by the loading particles. The detailed look of the sandy ballast bed is shown in Fig. 12 (d).

When developing the sand ballast bed model, the volume of the voids in the ballast bed is counted by the fish language, and the number of sand particles required is calculated. After that, the sand particles are equally divided into 10 parts and filled into the ballast bed in 10 times. After each filling, the model is fully balanced under gravity. When the unbalanced force of the particles is less than 1×10^{-4}, the next filling is conducted. In this way, the voids in the ballast bed are almost fully filled by the sand particles. Finally, to model the sand particles accumulated above the ballast bed in the sandy railways (Fig. 3 (b)), some sand particles are randomly generated and fall freely on the top of the ballast bed.

The discrete element model adopts the wall boundary. The contact force is calculated according to the overlap between particles in the linear method following the studies in [22,23,43]. The displacement, velocity and acceleration of each particle are calculated using Newton's second law and motion differential equation. In this way, the contact forces and motion state of every particle can be continuously calculated and updated.
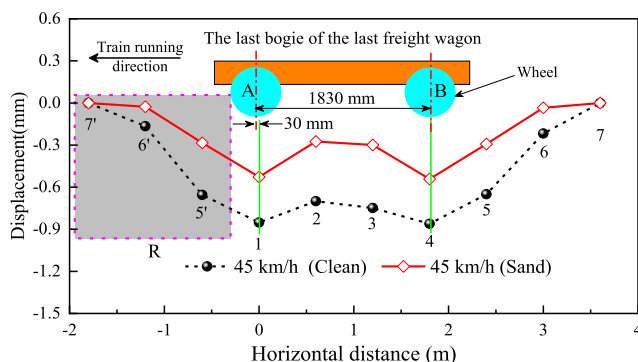

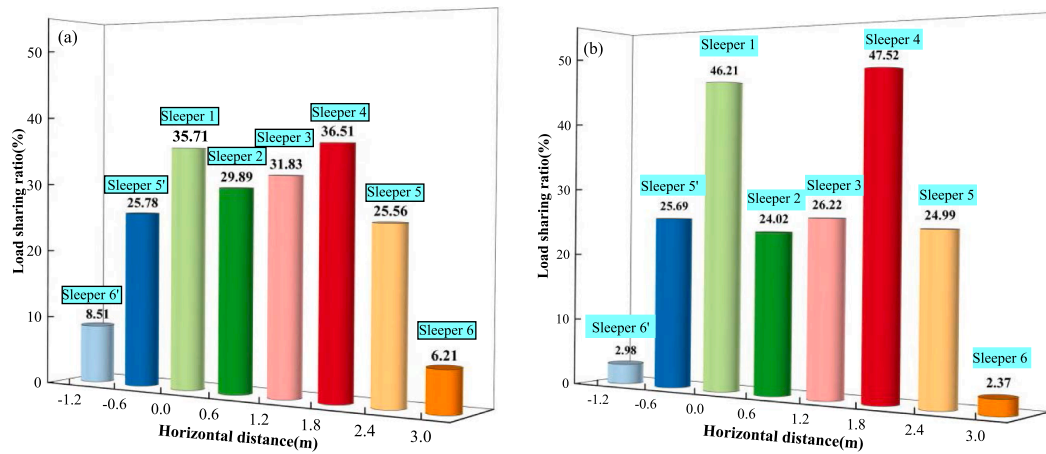**Fig. 9.** Sleeper displacement under the dual-axle load.

Fig. 10. Load sharing ratios of sleepers under the dual-axle load: (a) Clean section (45 km/h), (b) Sandy section (45 km/h).

Table 2
Load sharing ratios under sleeper in the dual-axle load.

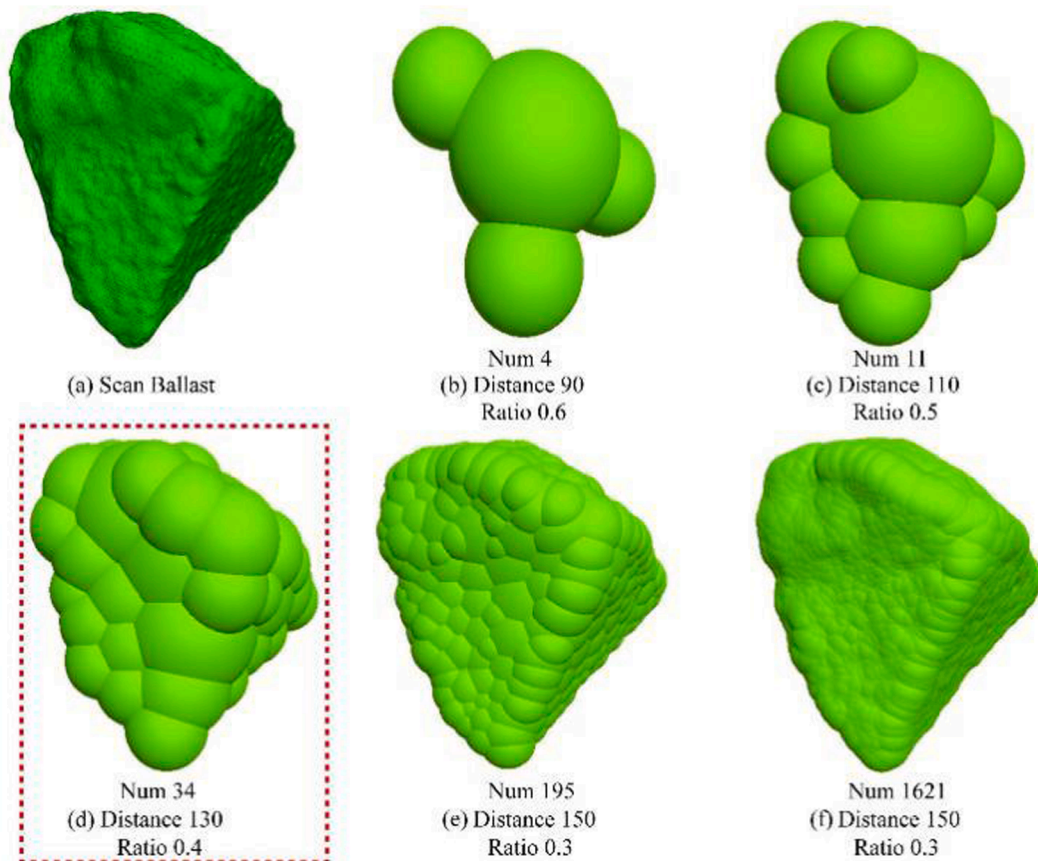| Section type	Load sharing ratios of sleeper							
	Sleeper 6′	Sleeper 5′	Sleeper 1	Sleeper 2	Sleeper 3	Sleeper 4	Sleeper 5	Sleeper 6
Clean	8.51%	25.78%	35.62%	29.89%	31.83%	36.51%	25.56%	6.21%
Sandy	2.98%	25.69%	46.21%	24.02%	26.22%	47.52%	24.99%	2.37%
Difference	−5.53%	−0.09%	10.50%	−5.87%	−5.61%	11.01%	−0.57%	−3.84%

Fig. 11. Formation process of ballast particle template.
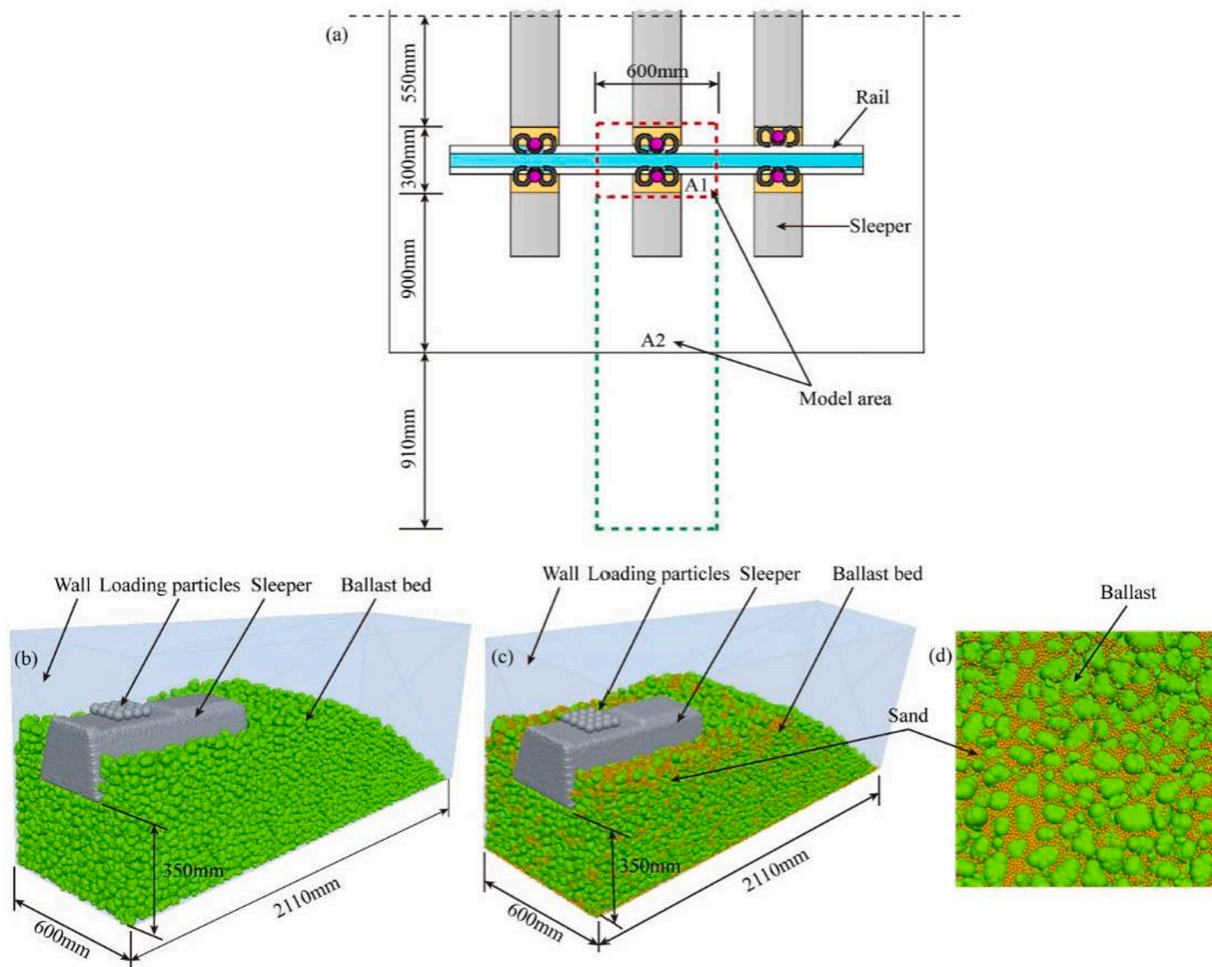
Fig. 12. Discrete element model: (a) Modelling area, (b) Model of clean ballast bed, (c) Model of sandy ballast bed, (d) Details of the model of sandy ballast bed.
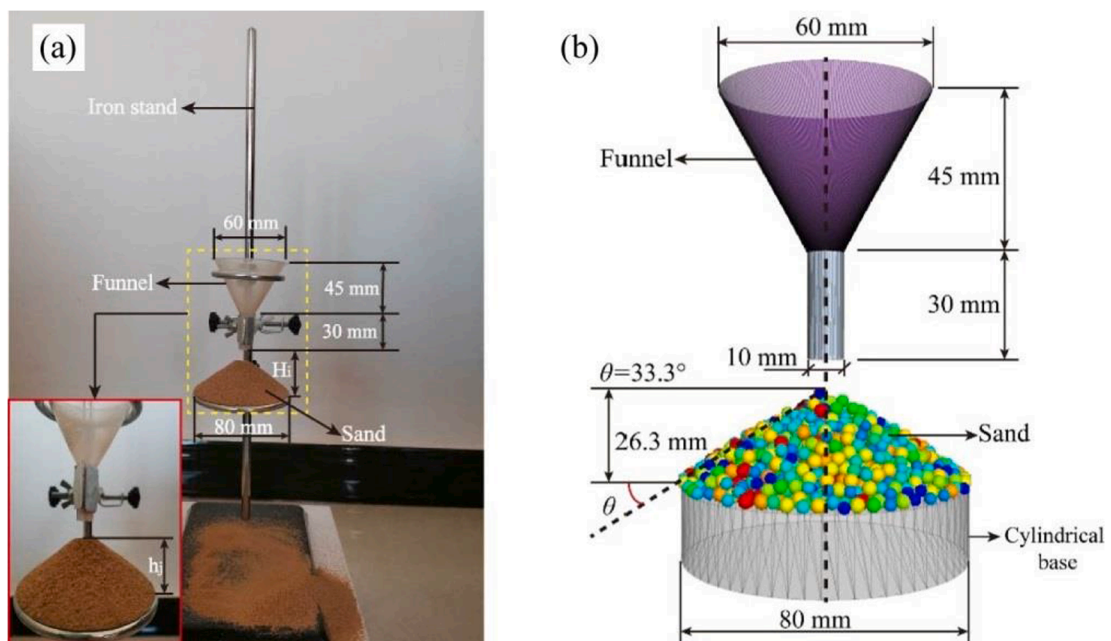

Fig. 13. Angle of repose: (a) Laboratory test, (b) Numerical simulation.

4.2. Parameter calibration and model validation

4.2.1. Angle of repose of sand

In order to obtain the contact parameters between sand particles, the laboratory test of the angle of repose of sand [24] has been performed as shown in Fig. 13, wherein three descending heights (H1, H2 and H3) have been tested. To avoid the interference of accidental factors on test results, each test has been repeated five independently. The sizes of sand particles ranged from 0.2 mm to 0.8 mm, with an average of 0.5 mm. The diameter D of the disk is 80 mm. The descending heights H_i are 100 mm, 50 mm and 35 mm, respectively. The angle of repose of sand is calculated using Eq. (4) and the results are shown in Table 3.

$$\theta = \frac{\sum_{i=1}^{5} arctan\frac{2H_i}{D}}{5} \tag{4}$$

As seen from Table 3, as the descending height H_i decreasing, the angle of repose of sand remains stable at about 33.0°. Considering the effect of descending height on the descending time in the discrete element simulation, the experimental results with the descending height of 35 mm (H3) and the angle of repose of 33.0° are used to calibrate the contact parameters for sand particles in the simulation.

To improve the computational efficiency of the discrete element model, following the existing research in [25,29], the size of sand particles is enlarged by 5 times in the numerical simulation of the angle of repose and the ball elements are used in the simulation as shown in Fig. 13 (b). The results of Cheng et al. [44] showed that the cohesive effect of dry sand is weak, while the friction and chain effect between particles are strong. Besides, the cohesive force is mainly generated by the interlock effect between particles. Therefore, the cohesive force between sand particles is not considered in this study, which follows [28] and the linear contact model is used for the calculation as shown in Fig. 14.

Because the contact between sand particles is composed of linear contact and damping contact [26], the contact force F^c can be decomposed into the linear contact force F^l and damping force F^d, as shown in Eq. (5). The linear contact force F^l can be calculated by the normal contact force F_n^l and tangential contact force F_s^l. The damping force F^d can be calculated by the normal damping force F_n^d and tangential damping force F_s^d, as shown in Eqs. (6) and (7).

$$F^c = F^l + F^d \tag{5}$$

$$F^l = F_n^l + F_s^l \tag{6}$$

$$F^d = F_n^d + F_s^d \tag{7}$$

The normal and tangential contact forces in Eq. (6) can be calculated from the relative displacement between particles and the normal contact stiffness k_n and tangential contact stiffness k_s as shown in Eqs. (8) and (9).

$$F_n^l = k_n x_n \tag{8}$$

$$F_s^l = (F_s^l)_0 - k_s \triangle x_s \tag{9}$$

Table 3
Test results of the angle of repose of sand.

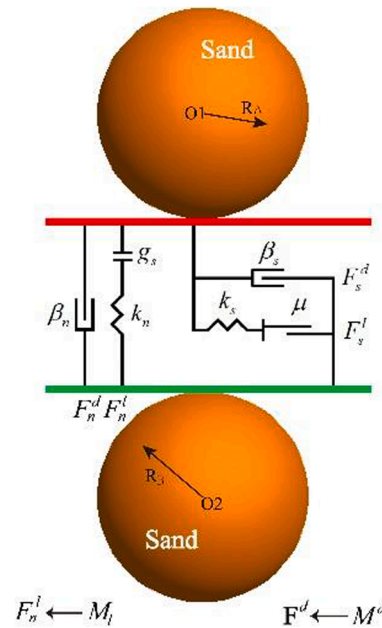| Stacking height (mm)	Descending height (mm)		
	$H_1 = 100$	$H_2 = 50$	$H_3 = 35$
h_1	30.0	29.0	27.0
h_2	26.0	26.0	26.0
h_3	24.0	26.0	25.0
h_4	23.0	26.0	26.0
h_5	26.0	26.0	26.0
Average value (mm)	25.8	26.6	26.0
Repose angle (°)	32.6	33.6	33.0

Fig. 14. Contact behaviour between sand particles.

where x_n is the normal relative displacement, $(F_s^l)_0$ is the tangential contact force in the initial state, and $\triangle x_s$ is the tangential displacement increment. The relationship between the normal and tangential contact forces of sand particles meet the Molar Coulomb Slip Criterion [22]. When the tangential contact force of sand particles reaches the shear strength, the relative slip occurs between particles, as shown in Eq. (10).

$$F_s = -\mu F_n \tag{10}$$

The damping contact force F^d is composed of the normal damping force F_n^d and tangential damping force F_s^d, which can be calculated by Eqs. (11) and (12).

$$F_n^d = (2\beta_n \sqrt{m_c k_n})\dot{\delta}_n \tag{11}$$

$$F_s^d = (2\beta_s \sqrt{m_c k_s})\dot{\delta}_s \tag{12}$$

where β_n and β_s are the normal and tangential critical damping ratios, respectively, $\dot{\delta}_n$ and $\dot{\delta}_s$ are the normal and tangential relative velocities, respectively [27], and m_c is the effective inertial mass. The contact stiffness k_n and k_s between sand particles can be calculated by the effective contact modulus E_c, the contact stiffness ratio k^*, and the radius of adjacent particles R_A and R_B [28], as shown in Eqs. (13) and (14).

$$k_n = \frac{\pi r^2 E_c}{R_A + R_B} \tag{13}$$

$$k_s = k_n/k^* \tag{14}$$

where r is the minimum of radius R_A and R_B and r takes half of the average particle size as 1.25 mm since the simulated sand particle size is small, the effective elastic modulus E_c is 1×10^8 Pa [28], and k^* is taken as 4.0/3. After calculation, it has been found that the normal and tangential contact stiffness of sand particles are 2.0×10^5 N/m and 1.5×10^5 N/m, respectively. To simulate the test of the angle of repose, the normal and tangential contact stiffness between the funnel and the sand particles are taken as 1.0×10^8 N/m and 1.0×10^8 N/m, respectively, and friction coefficients as 0.1. Several values for the friction coefficient between sand particles have been tested including 0.4, 0.45, 0.5, 0.55, 0.6, 0.65 and 0.7. It has been found that when the friction coefficient between sand particles is 0.65, the angle of repose is 33.3°, which is very

close to the test result. Note that a difference of 0.3° is within the allowable error range. In this way, the contact parameters have been selected which can reflect the interaction between the sand particles accurately and thus is used for further analysis.

4.2.2. Model validation

According to the test of the angle of repose and the existing research in [30–32,42,45], the contact parameters in the discrete element model are determined, as shown in Table 4. Because the sand particles and ballast particles are different types of granular materials, there is a great difference in contact stiffness and friction coefficient. To accurately calculate the contact forces between ballast and sand, the reference [27] obtains the effective contact parameters between sand and ballast with the help of the attribute inheritance principle.

To validate the discrete element model, the time-history curve of sleeper pressure obtained in the field test (discussed in Section 2.2, and shown in Fig. 15) is used as the input for the sandy ballast bed model (discussed in Section 4.1). During the calculation, the time step is determined in the following way to ensure the stability and reliability of the results. Firstly, the maximum time step is calculated by the fish language according to the characteristics of particle size, density, and stiffness. Secondly, the maximum time step is multiplied by the time step reduction coefficient of 30%. Finally, the time step is determined to be 1.5×10^{-8} s. The comparison between the simulation results and the numerical results is shown in Fig. 16, wherein both sleeper displacements and ballast bed acceleration are presented.

As seen from Fig. 16 (a), the curve of sleeper displacement calculated by the simulation matches well with the test result. The sleeper displacements of the simulation and test are similar under each wheel. As seen from Fig. 16 (b), the accelerations in the ballast bed of the test results are between 0.73 g and 0.79 g, and that of the simulation result between 0.69 g and 0.76 g, the difference of which ranges from 2.7% to 8.0%, with an average of 4.65%. Therefore, it can be concluded that the sleeper displacements and the ballast bed accelerations of the test and simulation are very similar. It shows that the numerical model can be used for further analysis of the interaction between sand and ballast particles.

4.3. Result analysis

4.3.1. Contact force between ballast particles

Contact forces between ballast particles in the ballast bed is an important index to reflect the mechanical behaviour of the ballast bed. To study the effect of sand intrusion on the contact force, the spatial distribution of the contact force between ballast particles in the clean and sandy ballast beds under the train load are plotted by the Tecplot 360, as shown in Fig. 17. The colours of arrows in Fig. 17 indicate the level of contact forces.

As seen from Fig. 17, the contact forces in the ballast bed at the bottom of the sleeper are larger, and that in the clean section is less than the sandy section. The maximum contact force in the sandy section is 1107 N, which is 80.29% higher than that in the clean section. The reasons are as follows. Firstly, the load sharing ratio of the sleeper in the sandy section is larger. Secondly, the sand intrusion limits the movement and rotation of ballast particles so that the stress in the ballast is difficult

Table 4
Parameters of the discrete element model.

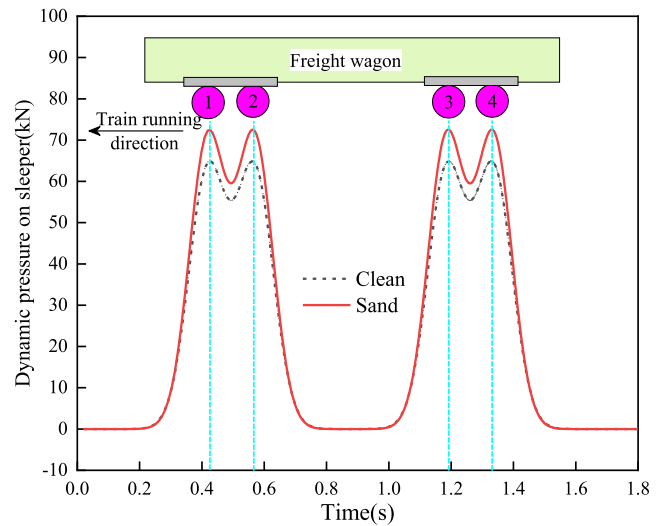| Parameter	Value
Density of ballast particles / (kg/m³)	2600
Density of sand particles / (kg/m³)	2650
Normal/tangential contact stiffness of ballast particles / (N/m)	5×10^7
Friction coefficient of ballast particles	0.55
Normal/tangential contact stiffness of sand particles/ (N/m)	$2.0 \times 10^5 / 1.5 \times 10^5$
Friction coefficient of sand particles	0.65

Fig. 15. Sleeper pressure test value.

to redistribute. In addition, the number of contacts between ballast particles and sleeper as well as between ballast particles and ballast particles decreases as indicated by fewer arrows in Fig. 17 (b), which is also caused by the sand intrusion.

To further analyze the influence of sand intrusion on the contact state inside the ballast bed, the probability density of normal and tangential contact force of ballast particles and coordination number under the train load are calculated, as shown in Fig. 18.

As seen from Fig. 18 (a), the probability density of normal and tangential contact forces both in the clean and sandy ballast beds falls gradually with the increase of contact forces, showing the most ballast particles in the ballast beds are at a low-stress level. The comparison shows that the normal and tangential contact forces in the sandy section are both larger than those in the clean section. The maximum normal contact force is about 2.5 times larger than the maximum tangential contact force, which is closely related to the magnitude and direction of the load on the sleeper.

As seen from Fig. 18 (b), the coordination number of the ballast bed in the sandy section shows an inverted "L" shape, while that in the clean section shows a "semi-elliptical" shape. The maximum coordination number in the sandy section is 85, with an average and variance of 13 and 64.7, respectively, which is 2.40, 0.63, and 2.72 times compared to that in the clean section. This shows that the sand intrusion changes the contact state between ballast particles and enhances the constraint effect of single ballast. However, the variance of the coordination number of ballast particles in the ballast bed also becomes larger, which increases the discreteness of the constraint of ballast particles. This also indicates the contact state of the ballast particles in the sandy section becomes more complex, in other words, the anisotropy of contact is stronger.

4.3.2. Displacement of ballast particles

The displacement and movement direction of ballast particles determine the cumulative settlement and deformation of ballast beds [33]. Under the action of train loads, the crushing and abrasion of ballast particles change the spatial motion of ballast particles. With the effect of the sand instruction, the porosity in the ballast beds becomes smaller and the contact points of ballast particles increase. Consequently, the displacement of ballast particles and the deformation of ballast beds become more complicated [34–35]. To study the effect of sand intrusion on the spatial motion of ballast particles, 6 cross-sections in the vertical direction in the ballast bed model are analysed. The thickness of each cross-section is 70 mm and the spacing between cross-sections is 200 mm. Besides, 3 cross-sections in the lateral direction are analysed, with a thickness of 70 mm and a spacing of 175 mm. The displacement of
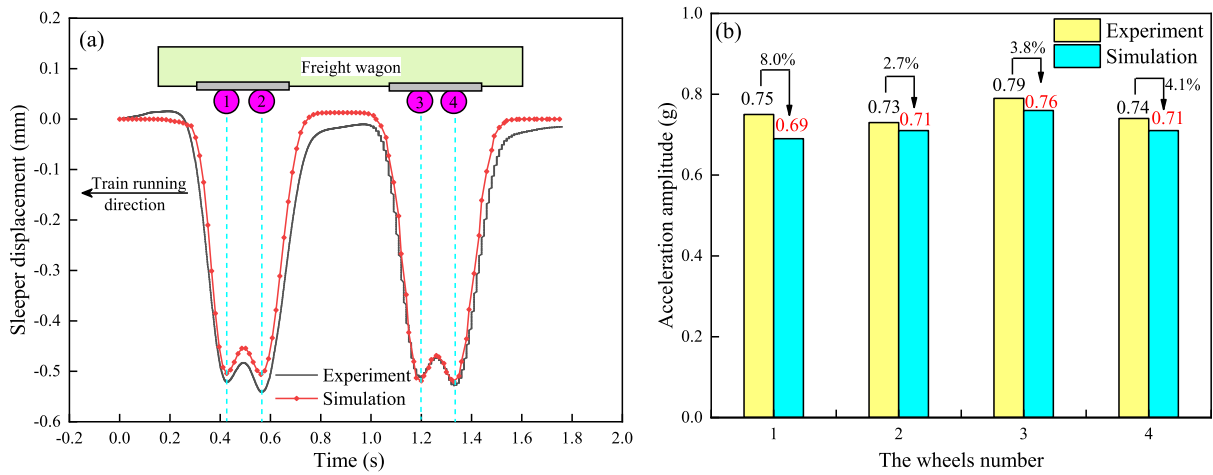
Fig. 16. Comparison between the test and simulation results: (a) Sleeper displacement, (b) Ballast bed acceleration.
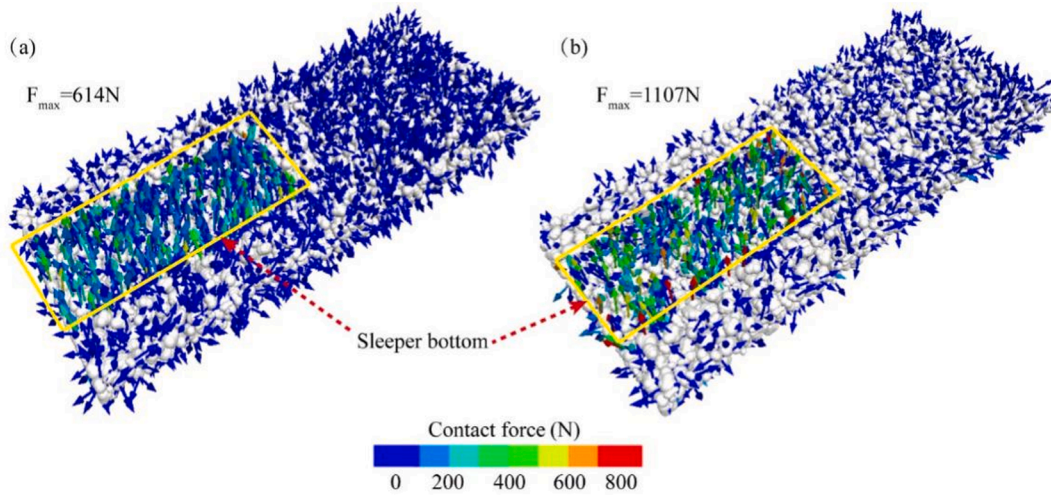

Fig. 17. Spatial distribution of contact force in the ballast beds: (a) Clean section (b) Sandy section.
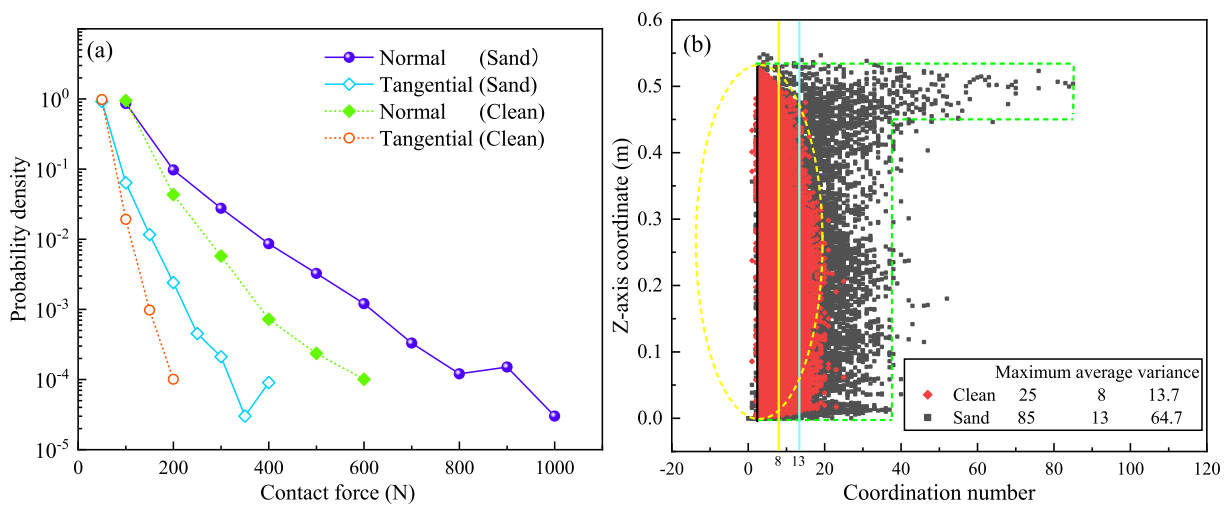

Fig. 18. Probability density of contact force and coordination number: (a) Probability density of normal and tangential contact force, (b) Coordination number.

ballast particles in the 6 vertical cross-sections, including amplitude and direction, are collected using the fish language, as well as the vertical displacement of ballast particles in the 3 lateral cross-sections in both the clean and sandy sections are shown in Figs. 19 and 20, respectively.

From Fig. 19 and Fig. 20, it can be seen that in the vertical direction of the ballast bed, the ballast bed under the sleeper in the clean and
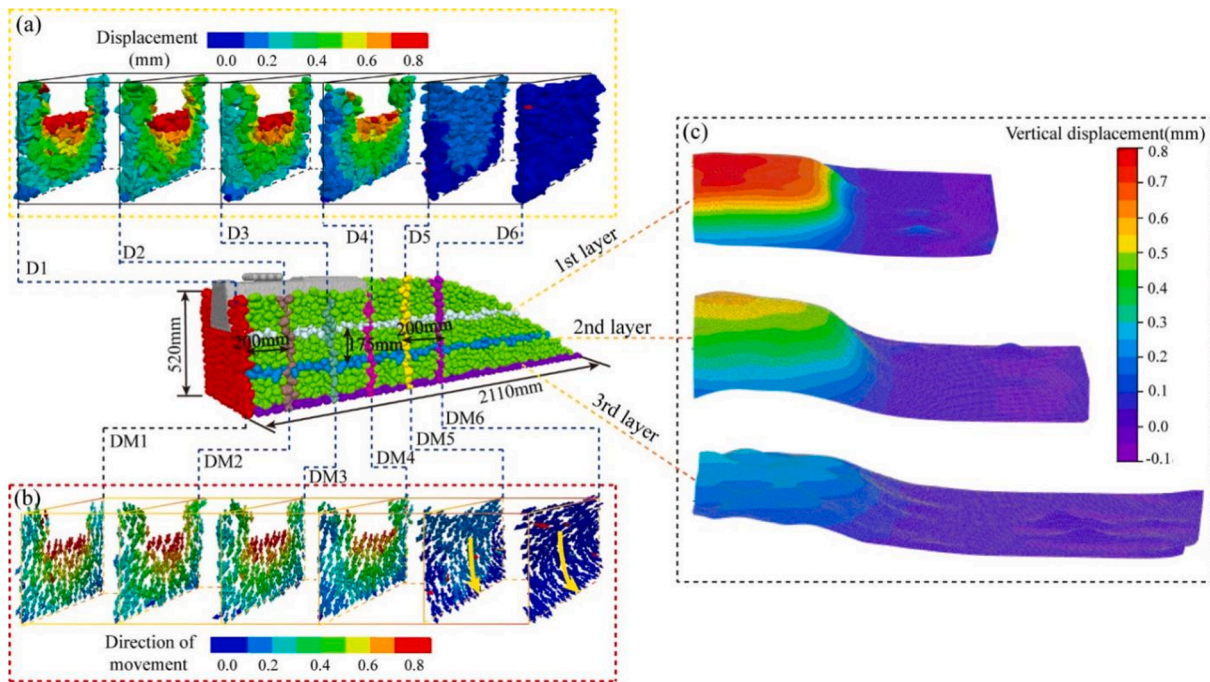
Fig. 19. Displacement of ballast particles in clean section: (a) Amplitude of displacement in the 6 vertical cross-sections; (b) Direction of displacement in the 6 vertical cross-sections, (c) Vertical displacement in the 3 lateral cross-sections.

Fig. 20. Displacement of ballast particles in sandy section: (a) Amplitude of displacement in the 6 vertical cross-sections, (b) Direction of displacement in the 6 vertical cross-sections, (c) Vertical displacement in the 3 lateral cross-sections.
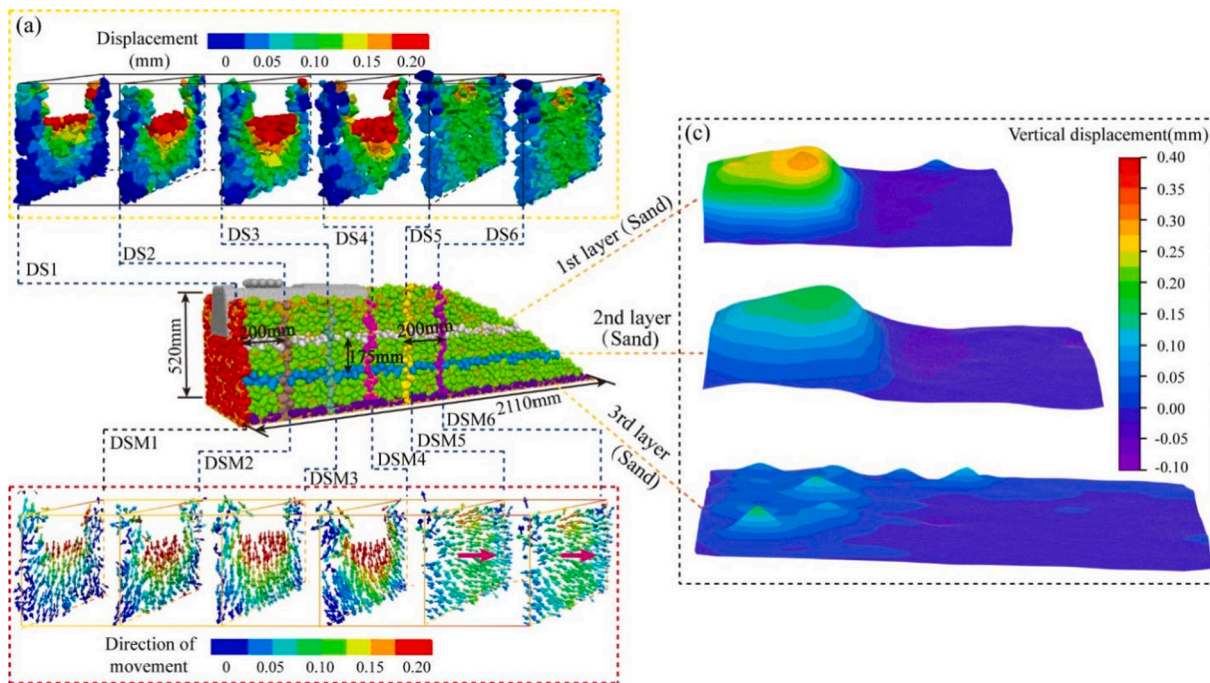
sandy sections mainly moves vertically and the displacements under the load are larger than other locations. As deeper from the bottom of the sleeper, the displacements of ballast particles decrease gradually and the contour of the displacements has a fan shape. This shows that the load is distributed from the sleeper to the ballast bed. By comparing the 6 cross-sections, it can be seen that the displacements under the load (the loading particles) are larger, and gradually reduces from the center to both sides. It shows that the displacement of ballast particles at the ballast shoulder is significantly smaller than that under the sleeper.

Besides, the direction of the displacements at the ballast shoulder is different from that under the sleeper.

Comparing Fig. 19 with Fig. 20, it can be found that the maximum displacement of ballast particles in the clean section is 0.8 mm, which is about 4 times larger than that in the sandy section. The ballast particles at the ballast shoulder move downward in the direction of less than 45°, while those in the sandy section move outward at 90°. This shows that sand intrusion limits the movement of ballast particles, which is consistent with the findings in references [7,41]. However, the sand

intrusion may cause ballast rheology at the lower part of the ballast shoulder, which is harmful to the stability of the slope of the ballast bed. Therefore, the sand intrusion of the ballast shoulder should be carefully considered during the track maintenance of ballast beds and remove if necessary.

4.3.3. Energy dissipation

Ballast beds have strong non-linearity and the energy dissipation in ballast beds is irreversible. The movement, abrasion and crushing of ballast particles are all accompanied by the storage, migration, dissipation of energy [21,36]. The sand intrusion intensifies the anisotropy of ballast particles, causing that the energy dissipation process more complex and the mechanical behaviour of ballast beds more unstable. According to the law of thermodynamics [37], the energy in ballast beds mainly contains the following parts, as shown in Eq. (15).

$$\triangle W = \triangle E_s + \triangle E_d + \triangle E_f + \triangle E_b + \triangle E_k + \triangle E_g \tag{15}$$

where $\triangle W$ is the input energy of train loads, $\triangle E_s$ is the elastic strain energy, $\triangle E_d$ is the damping energy including the local damping energy $\triangle E_{d1}$ and contact damping energy $\triangle E_{d2}$, $\triangle E_f$ is the friction energy between particles, $\triangle E_b$ is the energy consumed by particle breakage and damage, $\triangle E_k$ is the kinetic energy of particles, and $\triangle E_g$ is the body energy of particles. Because ballast and sand particles are hard, they are considered as unbreakable bodies under a single train load. Thus, the energy consumed by particle crushing and damage is ignored ($\triangle E_b = 0$). Therefore, Eq. (15) can be simplified as follows.

$$\triangle W = \triangle E_s + \triangle E_d + \triangle E_f + \triangle E_k + \triangle E_g \tag{16}$$

To accurately calculate the effect of sand intrusion on the energy dissipation in the ballast bed, the error caused by the uncompacted particles during the first loading process should be avoided. Therefore, the loading process is divided into 6 stages and only the stable stages are used for analysis as shown in Fig. 21. The stages of the loading process include: (1) Stage 1 from Point A to B is the stage before loading; (2) Stage 2 from Point B to C is the stage loaded by Wheel 2; (3) Stage 3 from Point C to D is the stage unloaded by Wheel 2; (4) Stage 4 from Point D to E is the stage loaded by Wheel 1; (5) Stage 5 from Point E to F is the stage unloaded by Wheel 1; (6) Stage 6 from Point F to G is the unloading stage.

To study the influence of sand intrusion on each energy component in the ballast bed under the load, elastic strain energy $\triangle E_s$, particle kinetic energy $\triangle E_k$, friction energy $\triangle E_f$, damping energy $\triangle E_d$ and particle body energy E_g are calculated respectively. Because E_g is very small, it can be ignored in the calculation. The calculation method of $\triangle E_s$ in the ballast bed is shown in Eq. (17).

$$\triangle E_s = \frac{1}{2} \sum_{i=1}^{N_c} \left(\frac{F_n^{i2}}{k_n} + \frac{F_s^{i2}}{k_s} \right) \tag{17}$$

In which, F_n^i and F_s^i are the normal force and tangential force of the ith particle respectively, k_n and k_s are normal and tangential stiffness, respectively, N_c is the number of contacts between particles.

The kinetic energy $\triangle E_k$ in the ballast bed can be calculated as follows:

$$\Delta E_k = \sum_{i=1}^{N_p} \triangle e^i \tag{18}$$

$$\Delta e^i = \frac{1}{2} \left\{ m_i(v_i^2 - v_0^2) + I_i(\omega_i^2 - \omega_0^2) \right\} \tag{19}$$

where N_p is the number of particles, $\triangle e^i$ is the kinetic energy of the ith particle, m_i is the mass of the ith particle, v_i is the current translation speed of the ith particle, v_0 is the initial velocity of particles, I_i is the rotational inertia of the ith particle, ω_i is the rotational speed of the ith particle, and ω_0 is the initial rotational speed of particles.

The friction energy $\triangle E_f$ in the ballast bed can be calculated as follows.

$$\triangle E_f = \sum_{j=1}^{H} \triangle E_f^j \tag{20}$$

$$\triangle E_f^j = \sum_{i=1}^{N_c} \langle F_s^i \rangle \triangle X_{s\mu}^i \tag{21}$$

where H is the total time step of the calculation, N_c is the number of contacts between particles, $\triangle E_f^j$ is the friction energy in a time step, $\langle F_s^i \rangle$ is the average tangential force in a time step, and $\triangle X_{s\mu}^i$ is the increment of the slip displacement between particles in a time step.

The damping energy $\triangle E_d$ can be calculated by Eqs. (22) and (23) as follows.

$$F^d = -c\dot{\delta} \tag{22}$$

$$\triangle E_\beta = F^d \dot{\delta} \triangle t \tag{23}$$

where F^d is the damping force between particles, c is the damping coefficient, $\dot{\delta}$ is the relative velocity between particles, and $\triangle t$ is the action time of damping force [37].

The energy components in the ballast bed in the clean and sandy ballast beds are shown in Fig. 22.

As seen from Fig. 22, the elastic strain energy and kinetic energy of the ballast bed experiences a process of increase–decrease-increase–decrease, while the friction energy and damping energy first increase and then stabilize gradually. Note that the increase of the damping energy in the clean ballast bed is smaller than that in the sandy ballast bed. This shows that the damping of the ballast bed is increased by the sand intrusion.

The elastic strain energy is one of the main indexes to access the elastic performance of ballast beds. As seen from Fig. 22 (a), the elastic strain energy in the clean ballast bed is always larger than that in the sandy ballast bed (Stage 2 ~ Stage 5) during the train load. The maximum elastic strain energy in the clean ballast bed is 26.76 J, while that in the sand track is 8.70 J, which is only 32.51% of the former. This means the elasticity of the sandy ballast bed is low. It is because the voids in the ballast bed are filled by the sand particles, changing the ballast grading and increasing the stiffness of the ballast bed.

The kinetic energy is an index to access the intensity of particle movement in ballast beds. As seen from Fig. 22 (b), the magnitude of the kinetic energy in the ballast bed is 10^{-3} J, which is at least 1000 times smaller than other types of energy. How it can still show the influence of
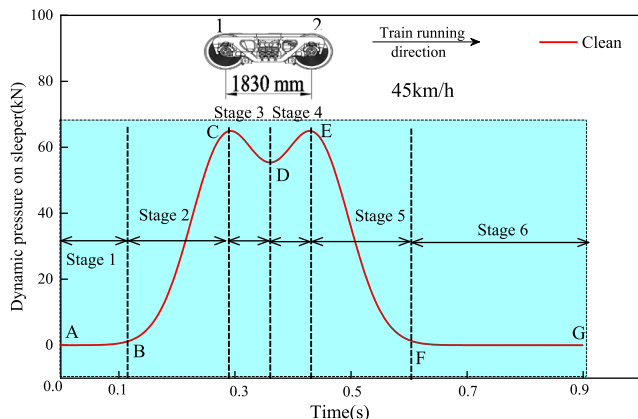

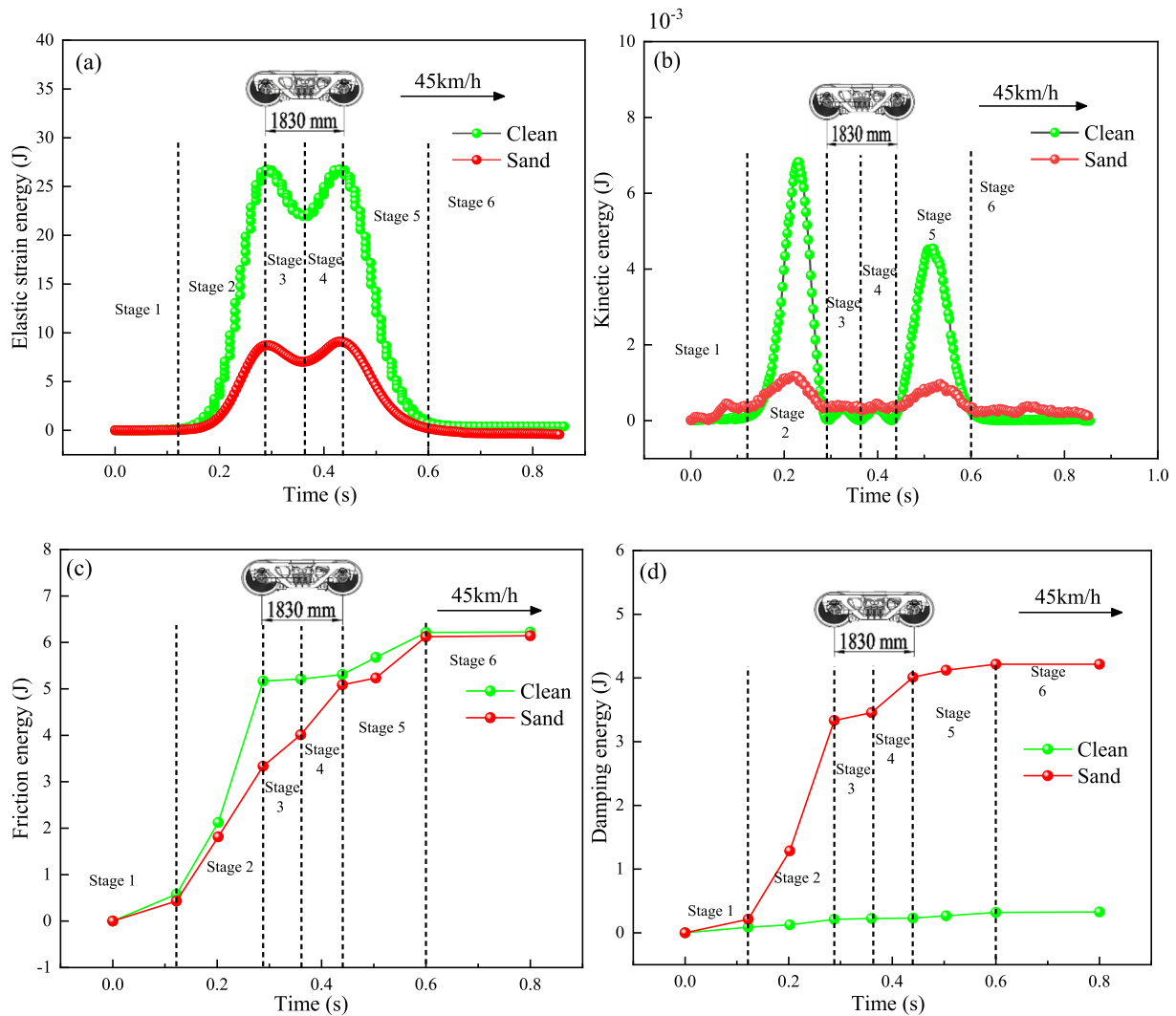**Fig. 21.** Sleeper pressure segments.

Fig. 22. Energy of the ballast bed: (a) Elastic strain energy, (b) Kinetic energy, (c) Friction energy, (d) Damping energy.

sand particles on the movement of ballast particles. By comparison, it can be seen that the kinetic energy in the clean and sandy ballast beds are increased in Stage 2 and Stage 5, while remaining stable in other stages. This is because during the loading process the compressive force between ballast particles increases gradually, while the unbalanced force of ballast particles firstly increases and then decreases. As a result, when the mass of ballast particles is constant, the acceleration also firstly increases and then decreases, and so as the velocity. Besides, in Stage 2 and Stage 5, the kinetic energy in the sandy ballast bed is significantly less than that in the clean ballast bed, which is because the sand intrusion increases the coordination number of ballast and enhances the restraint.

The friction energy is generated due to the relative sliding between particles, which is one of the most important ways of energy dissipation. As seen from Fig. 22 (c), during the whole loading process, the friction energy in the clean ballast bed is larger than that in the sandy ballast bed, especially in Stage 2, 3 and 4, which indicates that the ballast particles in the sandy ballast bed are less easy to slip due to the strong restraint.

The damping energy is one of the important indexes to access energy dissipation. As seen from Fig. 22 (d), the damping energy in the sandy ballast bed increases slowly in Stage 1, rapidly in Stage 2 and later slowly again in Stage 3. After that, the growth rate of damping energy in the sandy ballast bed gradually reduces to none in Stage 4–6. On the contrary, the damping energy in the clean ballast bed is significantly

lower in all stages. The maximum damping energy in the sandy ballast bed is 4.22 J, which is about 13.2 times that in the clean ballast bed. This shows that the energy dissipation capacity of the ballast bed is significantly enhanced by the sand intrusion. It is because the number of contacts between particles in the ballast bed is considerably increased by the sand intrusion, and thus the cumulative of contact damping is increased remarkably. As a result, the sand ballast bed shows a strong capacity for energy dissipation.

In summary, the sand intrusion strongly affects the elastic strain energy and damping energy in the ballast bed, but has less effect on friction energy and kinetic energy.

5. Conclusions

Based on the field test of the load sharing ratio of sleepers, the laboratory test of the angle of repose of sand, and numerical simulation using the three-dimensional discrete element model of the track with the sand intrusion, the paper studies the load sharing ratio of sleepers in both the clean and sandy track under the single-axle load and dual-axle load, the influence of sand intrusion on the contact force, the movement pattern of ballast particles and energy dissipation in the ballast bed. The conclusions are as follows:

(1) A single-axle load on the sandy track is mainly carried by three sleepers, the load sharing ratios of which are 1.3:2.4:1.3. In the

case of a dual-axle load, the load on the sandy track is mainly carried by 6 sleepers, the load sharing ratios of which are 2.6:4.7: 2.5:4.9:2.6. The load sharing ratio of sleepers directly under the single-axle load is smaller than that under the dual-axle load. Thus, the dual-axle load (a bogie) is recommended to use as train loads in the design of sandy railway lines.

(2) By conducting the angle of repose tests, it is obtained that the angle of repose of sand is 33.0° and the friction coefficient between sand particles is 0.65. Besides, it has been found that the particle size can be enlarged by 5 times in the simulation to improve the computational efficiency while reasonable results can still be achieved.

(3) The maximum contact force under the sleeper in the sandy ballast bed is about 80% higher than that in the clean ballast bed. The normal and tangential contact forces are also larger than that in the clean ballast bed. The sand intrusion changes the stiffness of ballast beds and increases the load applied on ballast beds. Moreover, the coordination number in the sandy ballast bed shows an inverted "L" shape, while that in the clean ballast bed shows a "semi-elliptical" shape, indicating that the anisotropy of the contact is stronger in the sandy ballast bed.

(4) The displacements of ballast particles in the clean ballast bed are much less than that in the sandy ballast bed. The ballast particles at the ballast shoulder move downward in the direction of less than 45°, while those in the sandy ballast bed move outward at 90°. The sand intrusion can inhibit the movement of ballast particles and may cause lateral flow of ballast shoulders, which is harmful to the stability of the slope of ballast beds and therefore should be carefully considered during track maintenance.

(5) Sand intrusion mainly affects the elastic strain energy and damping energy in ballast beds but has less effect on friction energy and kinetic energy. During train loads, the elastic strain energy, kinetic energy and friction energy in the sandy ballast bed all decrease, while the damping energy increases.

CRediT authorship contribution statement

Hong Xiao: Project administration, Funding acquisition, Supervision. **Zhihai Zhang:** Conceptualization, Methodology, Formal analysis, Writing – original draft. **Yihao Chi:** Software, Validation, Formal analysis. **Meng Wang:** Software, Data curation. **Haoyu Wang:** Writing – review & editing.

Declaration of Competing Interest

The authors declare that they have no known competing financial interests or personal relationships that could have appeared to influence the work reported in this paper.

Acknowledgements

References

[1] E.T. Selig, J.M. Waters, Track geotechnology and substructure management, Thomas Telford, London, 1994.

[2] E. Tutumluer, W. Dombrow, H. Huang. Laboratory characterization of coal dust fouled ballast behavior [C]. Nashville: AREMA 2008 Annual Conference & Exposition September, 2008: 21-24.

[3] L. Bruno, M. Horvat, L. Raffaele, Windblown sand along railway infrastructures: A review of challenges and mitigation measures, J. Wind Eng. Ind. Aerodyn. 177 (2018) 340–365.

[4] A.R.T. Kian, J. Sadeghi, J.A. Zakeri. Large-scale direct shear tests on sand-contaminated ballast. Proceedings of the Institution of Civil Engineers-Geotechnical Engineering, 2018, 171(5): 451-461.

[5] K.-C. Zhang, J.-J. Qu, K.-T. Liao, Q.-h. Niu, Q.-J. Han, Damage by wind-blown sand and its control along Qinghai-Tibet Railway in China, Aeolian Res. 1 (3-4) (2010) 143–146.

[6] A.R.T. Kian, J.A. Zakeri, J. Sadeghi, Experimental investigation of effects of sand contamination on strain modulus of railway ballast, Geomechanics and Engineering 14 (6) (2018) 563–570.

[7] J.A. Zakeri, R. Abbasi, Field investigation of variation of loading pattern of concrete sleeper due to ballast sandy contamination in sandy desert areas, J. Mech. Sci. Technol. 26 (12) (2012) 3885–3892.

[8] J.A. Zakeri, M. Esmaeili, M. Fathali, Evaluation of humped slab track performance in desert railways, Proceedings of the Institution of Mechanical Engineers, Part F: Journal of Rail and Rapid Transit 225 (6) (2011) 566–573.

[9] M. Koohmishi, M. Palassi, Effect of gradation of aggregate and size of fouling materials on hydraulic conductivity of sand-fouled railway ballast, Constr. Build. Mater. 167 (2018) 514–523.

[10] N. Tennakoon, B. Indraratna, C. Rujikiatkamjorn, S. Nimbalkar, T. Neville, The role of ballast fouling characteristics on the drainage capacity of rail substructure, Geotech. Test. J. 35 (4) (2012) 104107, https://doi.org/10.1520/GTJ104107.

[11] D. Ionescu, D. Fedele, Trounce M, et al. Deformation and degradation characteristics of sand-contaminated railway ballast. Proceedings of the third international conference on railway technology: research, development and maintenance. Civil-Comp Press, Stirlingshire. 2016.

[12] M. Esmaeili, J.A. Zakeri, S.A. Mosayebi, Effect of sand-fouled ballast on train-induced vibration, Int. J. Pavement Eng. 15 (7) (2014) 635–644.

[13] M. Esmaeili, P. Aela, A. Hosseini, Experimental assessment of cyclic behavior of sand-fouled ballast mixed with tire derived aggregates, Soil Dyn. Earthquake Eng. 98 (2017) 1–11.

[14] W.R. Tyfour, Effect of moving sand as a ballast contaminant on rail corrugation: field experience, Int. J. Environ. Eng. 6 (1) (2014) 15–28.

[15] J.-A. Zakeri, M. Esmaeili, S. Mosayebi, R. Abbasi, Effects of vibration in desert area caused by moving trains, J. Modern Transp. 20 (1) (2012) 16–23.

[16] A.R. Tolou Kian, J. Sadeghi, J.-A. Zakeri, Influences of railway ballast sand contamination on loading pattern of pre-stressed concrete sleeper, Constr. Build. Mater. 233 (2020) 117324, https://doi.org/10.1016/j.conbuildmat.2019.117324.

[17] China. TMOR. Railway Ballast (TB/T 2140-2008): Railway Industry Standard of the People's Republic of China, 2008.

[18] H. Liu, J. Xiao, P. Wang, G. Liu, M. Gao, S. Li, Experimental investigation of the characteristics of a granular ballast bed under cyclic longitudinal loading, Constr. Build. Mater. 163 (2018) 214–224.

[19] Ministry of Railways of the PRC, TB 10082-2017, Code design of railway track, China Railway Publishing House (2005). (in Chinese).

[20] L.Ü. Wenqiang, L.U.O. Qiang, L.I.U. Gang, et al., Structural analysis and design method for subgrade bed of heavy haul railway, J. China Railway Soc. 38 (4) (2016) 74–81 (in Chinese).

[21] M. Esmaeili, P. Aela, A. Hosseini, Effect of moisture on performance of mixture of sand-fouled ballast and tire-derived aggregates under cyclic loading, J. Mater. Civ. Eng. 31 (2) (2019) 04018377, https://doi.org/10.1061/(ASCE)MT.1943-5533.0002586.

[22] X. Ling, H. Xiao, G. Liu, M. Zhang, Discrete element modeling of polyurethane-stabilized ballast under monotonic and cyclic triaxial loading, Constr. Build. Mater. 255 (2020) 119370, https://doi.org/10.1016/j.conbuildmat.2020.119370.

[23] G. Jing, P. Aela, H. Fu, The contribution of ballast layer components to the lateral resistance of ladder sleeper track, Constr. Build. Mater. 202 (2019) 796–805.

[24] H. Nakashima, Y. Shioji, T. Kobayashi, S. Aoki, H. Shimizu, J. Miyasaka, K. Ohdoi, Determining the angle of repose of sand under low-gravity conditions using discrete element method, J. Terramech. 48 (1) (2011) 17–26.

[25] L. Widulinski, R. Kozicki, R. Tejchman, Numerical simulations of triaxial test with sand using DEM, Arch. Hydroengineering Environ. Mech. 56 (3–4) (2009) 149–172.

[26] P.A. Cundall, O.D.L. Strack, A discrete numerical model for granular assemblies, Géotechnique 30 (3) (2008) 331–336.

[27] Itasca Consulting Group Inc. PFC 5.0 documentation, User's Guide. Minneapolis. (2015).

[28] J. Gong, Z. Nie, Y. Zhu, Z. Liang, X. Wang, Exploring the effects of particle shape and content of fines on the shear behavior of sand-fines mixtures via the DEM, Comput. Geotech. 106 (2019) 161–176.

[29] S. Iai, T. Tobita, T. Nakahara, Generalised scaling relations for dynamic centrifuge tests, Géotechnique 55 (5) (2005) 355–362.

[30] W. Jia, V. Markine, Y. Guo, G. Jing, Experimental and numerical investigations on the shear behaviour of recycled railway ballast, Constr. Build. Mater. 217 (2019) 310–320.

[31] A. Danesh, A.A. Mirghasemi, M. Palassi, Evaluation of particle shape on direct shear mechanical behavior of ballast assembly using discrete element method (DEM), Transp. Geotech. 23 (2020) 100357, https://doi.org/10.1016/j.trgeo.2020.100357.

[32] G. Jing, X. Zhang, W. Jia, Lateral resistance of polyurethane-reinforced ballast with the application of new bonding schemes: Laboratory tests and discrete element simulations, Constr. Build. Mater. 221 (2019) 627–636.

[33] H. Huang, S. Chrismer, Discrete element modeling of ballast settlement under trains moving at 'Critical Speeds, Constr. Build. Mater. 38 (2013) 994–1000.

[34] E. Mahmoud, A.T. Papagiannakis, D. Renteria, Discrete Element Analysis of Railway Ballast under Cycling Loading[J], Procedia Eng. 143 (2016) 1068–1076.

[35] S. Lobo-Guerrero, L.E. Vallejo, Discrete element method analysis of railtrack ballast degradation during cyclic loading, Granul Matter 8 (3-4) (2006) 195–204.

[36] Y.P. Cheng, Y. Nakata, M.D. Bolton, Micro and macro-mechanical behavior of DEM crushable materials, Géotechnique 58 (58) (2008) 471–480.

[37] Hong Xiao, Zhihai Zhang, Xuhao Cui, et al., Experimental study and discrete element analysis of ballast bed with various sand content, Constr. Build. Mater. 271 (2021).

[38] J. Sadeghi, A.R. Tolou Kian, H. Ghiasinejad, M. Fallah Moqaddam, S. Motevalli, Effectiveness of geogrid reinforcement in improvement of mechanical behavior of sand-contaminated ballast, Geotext. Geomembr. 48 (6) (2020) 768–779.

[39] Sadeghi Javad, Tolou Kian Ali Reza, Fallah Mosarreza. Experimental Investigation of Mechanical Properties of Ballast Contaminated with Wet Sand Materials. 2020 American Society of Civil Engineers. DOI: 10.1 061 /(ASCE) GM .1943-5622.0001886.

[40] Z. Zhang, H. Xiao, H. Cui, et al., Multi-scale model establishment and mechanical analysis of railway ballast bed in sandstorm area, Journal of Central South University (Science and Technology) 52 (2) (2021) 635–647 (In Chinese).

[41] Z. Zhang, H. Xiao, M. Wang, M. Zhang, J. Wang, Research on dynamic mechanical behavior of ballast bed in windblown sand railway based on dimensional analysis, Constr. Build. Mater. 287 (2021) 123052, https://doi.org/10.1016/j.conbuildmat.2021.123052.

[42] H. Xiao, Z. Zhang, X. Cui, F. Jin, Experimental study and discrete element analysis of ballast bed with various sand content, Constr. Build. Mater. 271 (2021) 121869, https://doi.org/10.1016/j.conbuildmat.2020.121869.

[43] H. Huang, E. Tutumluer, Discrete Element Modeling for fouled railroad ballast, Constr. Build. Mater. 25 (8) (2011) 3306–3312.

[44] X. Cheng, H. Qi, C. You, et al., Analyse of aeolian sandy physical characteristics in desert, J. Eng. Thermophys. 03 (2003) 437–440 (in Chinese).

[45] N.T. Ngo, B. Indraratna, C. Rujikiatkamjorn, DEM simulation of the behaviour of geogrid stabilised ballast fouled with coal, Comput. Geotech. 55 (2014) 224–231.